Computational Fluid Dynamics (CFD) Study of the Impact of Powered Air-Purifying Respirators (PAPR) in Underground Mining Operations

Luis Sanchez Gonzalez
The Pennsylvania State University,
University Park, PA

Barbara Arnold
The Pennsylvania State University,
University Park, PA

Ashish Ranjan Kumar
The Pennsylvania State University,
University Park, PA

ABSTRACT

Mining operations adopt a variety of measures to combat dust underground. These include ventilation systems, water sprays, physical barriers, and personal protective equipment (PPE). Respirators are a class of PPE that can provide clean particulate- free air to the users. Powered Air-Purifying Respirators (PAPRs), used commonly in medical and other sectors, are not prevalent in the mining industry. PAPRs use P100 filters that have 99.97% dust capture efficiency. We present our results from computational fluid dynamics (CFD) simulations performed to understand the impact of a PAPR on airflow and dust particle concentration in the vicinity of a miner. These results show that donning PAPRs can lower the miners' exposure to respirable coal dust in their workplace.

INTRODUCTION

Several processes in a mining facility generate dust particles. These include mechanical excavation of minerals, attrition during transportation, crushing, grinding, and others. Many of these particles have aerodynamic diameters of less than 10.0 μm. Most of them could be smaller than 4.0 μm in size. These particles are considered respirable [1]. They can travel deep inside the human respiratory system and cause irreversible illnesses in the affected persons. Mining operations, therefore, adopt several measures, such as artificial ventilation systems to dilute the particulate concentration under permissible limits. Water sprays are mounted at strategic locations within the mine. The sprays not only cool the cutting bits but also move the particles away from the miners using the higher airflow momentum. Flooded-bed dust scrubbers are installed on mining machines such as continuous miners. They capture dust particles on fibrous-type dust filters and are efficient under several conditions [2]. Recent research has also investigated the performance of novel non-clogging dust scrubbers, such as Vortecone and impingement-type dust filters. Unlike fibrous filters, these direct the motion of dust particles preferentially using their momentum and capture them on engineered surfaces. Their mechanical availability is much higher compared to traditional scrubbers [3; 4].

The scrubbers alleviate dust over a known flow domain. However, they are also attached to the major equipment and cannot protect the equipment operators or the miners who move continuously close to the active mining face. Therefore, personal protective devices (PPEs) are used to capture the dust particles and lower their exposure to respirable particulate matter. Powered Air-Purifying Respirators (PAPRs) are an important class of PPEs that have been demonstrated to capture 99.97% of airborne particles using P100-rated filters [5]. Therefore, they are used in hospitals and other settings where particulate exposure is critical to employee health. However, the mining industry has not adopted them on a large scale. This manuscript presents the operations of a PAPR using numerical modeling techniques. We developed computational fluid dynamics (CFD) models to show the steady-state airflow in the vicinity of the PAPR when placed in a controlled volume. We also present our findings from transient-state simulations that demonstrate particle transportation. We investigated particles of 1.0, 2.5, 4.0, and 10.0 μm. We used Reynold's-Averaged Navier-Stokes (RANS) turbulence models to develop these computer models.

LITERATURE REVIEW

Little information exists in the literature on CFD modeling of PAPRs. Section 2.1 provides a summary of PAPR operations. Section 2.2 describes some of the studies that were performed using CFD modeling.

PAPR OPERATIONS

A PAPR operates by capturing the dust-laden air from the vicinity of the user. A typical PAPR has (i) a battery-operated fan/blower/pump, (ii) a hose connecting the inlet to the pump, and (iii) a high- efficiency particulate air (HEPA) filter. The dust-laden air is brought into the system. The dust particles are trapped on the filter surface to provide clean air to the user [6]. The efficacy of PAPRs was demonstrated in several applications. Hospital personnel rely on HEPA and other filters to alleviate their exposure to minute micro-organisms that could be disease carriers [7]. Their efficiency was demonstrated during the coronavirus disease caused by the SARS-CoV-2 virus when surveys showed that 85% of healthcare workers in a hospital in Singapore preferred to use PAPRs instead of regular masks [8]. The performance of the PAPRs to capture the respirable dust particles is quantified in terms of 'Protection Factors (PFs).' The assigned protection factor for a PAPR with a loose- fitting hood or helmet is 25 [9]. Some of the most used PAPRs are the 3M Versaflo and the CleanSpace EX (Figure 1). In this paper, we present the results of airflow simulations using the 3M Versaflo Helmet.

Figure 1. 3M Versaflo (left) and CleanSpace EX (right) PAPRs

CFD MODELING OF PAPRS

CFD simulations of PAPRs have not been explored broadly. Very few studies exist in the literature that show the external airflow around a PAPR. However, some research shows the performance of different components of a PAPR separately. In one such work, particle transportation inside the mask was modeled using Open-FOAM software. It showed that leakage inside the mask increases as the particle size decreases [10]. Another CFD study showed experimentally validated results in terms of protection factors of up to 10,000 [11]. Pleated filters, such as the HEPA filters used in the PAPRs, have also been simulated. Some studies have focussed on finding the correlation between dust accumulation and pressure drop. A study shows that masks tend to achieve steady-state pressure with unique filter contamination percentages [12]. Another study shows that the pressure drop increases as dust accumulates in the filter [13]. An increased particle size also causes lower efficiency in the filter [14]. In summary, there are no studies that present modeling results using a replica of a PAPR or airflow and particulate transport around a miner using a PAPR.

SETTING UP THE CFD MODELS

We present results from CFD simulations of airflow and particle transportation around a miner's head. We selected a 3M Versaflo helmet for CFD simulations. For the simulations, we attached the geometry of the 3M Versaflo helmet to a human head model. This section will cover the parameters used to set up the simulations. We performed steady-state, transient- state, and particle-tracking simulations systematically to demonstrate the PAPR performance and five unique cases for every simulation by changing the inlet airflow velocity from 1.0 m/s to 3.0 m/s in increments of 0.5 m/s. This enables us to understand the impact of air velocity on particle behavior.

LIDAR SCAN FOR THE GEOMETRY

There are many techniques for 3D scanning, including photogrammetry and Light Detection and Range (LiDAR). These techniques allow the creation of a point cloud of the object, which can then be transformed into a faceted body and, finally, into a solid body. LiDAR was used for this study. Many modern phones have the technology that provides very accurate results. An iPhone 12 Pro and the mobile application KIRI were used to perform the scan. This can be used for photogrammetry or LiDAR; however, the limited number of photos that the application can process significantly affects the results.

The real 3M Versaflow helmet, generated point cloud, and faceted body are presented in Figure 2. To obtain a reliable solid body, some adjustments to the geometry were made to correct any mistakes during the 3D scanning process. Once the helmet geometry was ready, it was attached to a human head model downloaded from the GrabCAD library. The final geometry that was used is shown in Figure 3.

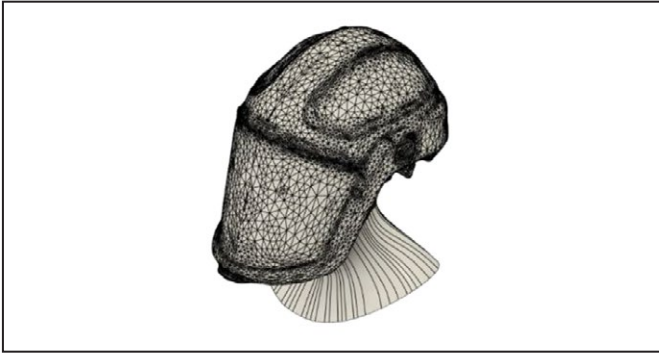**Figure 2. Real helmet (left), 3D points cloud (center), faceted body (right)**

Figure 3. The final geometry

MESH INDEPENDENCE

To perform CFD simulations, the flow volume must be discretized into fine grids, called mesh. It is one of the most important stages of simulation. A good quality mesh will provide accurate and reliable results. It also plays an important role in simulation convergence. Some important parameters are defined in Table 1; these thresholds were obtained from the operations manual of the ANSYS Fluent software [15]. The meshes developed for this research conform to the prescribed parameters.

a. **Aspect ratio**: It is the ratio between the height and width of the element. It ranges between 1 and infinite.
b. **Element quality**: This corresponds to the ratio between the volume and the square root of the cube of the sum of the edge lengths. It ranges between 0 and 1.
c. **Orthogonal quality**: It compares the vector between two nodes and the normal vector for each surface

integration point associated with the edge. It ranges between 0 and 1.
d. **Skewness**: It is the principal quality metric. It indicates how close an element is to an ideal equilateral or equiangular element. It ranges from 0 to 1.

After obtaining good quality meshes, it is important to establish mesh independence. This is critical to ensure that the simulation results are independent of the discretization scheme and the number of grid elements. For this, we compared three different meshes. These were categorized into coarse, medium, and fine classes depending on the average size of the grid elements. All meshes met the quality requirements. To compare the meshes, an average element size parameter was used. This was calculated by obtaining the cube root of the average grid volumes. The growth ratio of average element size across the three meshes was kept constant at about 1.3. The parameters for each mesh are shown in Table 2. The fluid volume was 1.26913 m^3.

Table 2. Element size calculations and mesh comparison

Parameters	Coarse	Medium	Fine
Element count (million)	1.101	2.481	5.325
Avg. volume [mm^3]	1,152	512	238
Avg. size [mm]	10.48	8.00	6.20
Cell count growth ratio	1.31	1.29	

Five probe points were placed around the helmet to compare the air velocity. A steady-state simulation with an inlet air velocity of 2.0 m/s was used for mesh independence studies. The results are shown in Table 3. As can be seen, there are no significant differences in velocities at those probe points. The biggest differences are found in places where recirculation is expected.

Table 3. Probe points velocities (m/s)

Locations	Coarse	Medium	Fine
v1 (Side 1)	2.35	2.36	2.35
v2 (Side 2)	2.35	2.35	2.37
v3 (Top)	2.43	2.44	2.47
v4 (Front)	1.51	1.34	1.4
v5 (Back)	1.65	1.8	1.96

With this information, the medium mesh will be selected, as it offers enough accuracy and is not too expensive computationally. The mesh quality metrics are shown in Table 4. Even if a few elements are not within the optimum range, quality is not bad enough to make the simulation fail or give inaccurate results. Once the mesh was

Table 1. Mesh quality parameters

Parameters	Threshold
Max aspect ratio	1,000
Min element quality	5e-4
Min orthogonal quality	5e-3
Max Skewness	0.999

Table 4. Mesh quality metrics

Parameters	Minimum	Maximum	Average	SD
Element quality	0.012	0.999	0.840	0.107
Aspect ratio	1.014	98.621	1.830	0.565
Orthogonal quality	0.006	1.000	0.775	0.135
Skewness	1.3e-10	0.994	0.223	0.137

defined, steady and transient-state CFD simulations were developed.

SIMULATIONS SET UP

Once the computational mesh was established, the following steps were followed to set up and run the CFD simulations. The simulations were run at Penn State's Institute of Computations and Data Science's (ICDS) supercomputing clusters.

Steady-state simulations: We used the RNG κ-ε turbulence model to solve the Navier-Stokes' equations using the medium mesh with about 2.48 million elements. The inlet was assigned to a normal velocity, and the outlet was assigned a 0 Pa static pressure. This pressure mimics its connection to the atmosphere. Inlet velocity magnitude was changed throughout the simulations. This assisted in identifying the zones where velocity is low, and particles may be trapped. Residuals were monitored with over 500 iterations. Reports were obtained for velocities at each of the five probe points added during the mesh independence studies.

Transient-state simulations and particle tracking: Different particle sizes were tested for the transient- state simulations to determine the ability of the PAPR to capture them. Simulations were developed to demonstrate the PAPR operations for 60.0 s as shown in Table 5. After 60.0 s, the percentage of the particles captured was calculated. The inlet velocity at the flow domain was set to 0.01 m/s to mimic a miner working in a closed volume such as a maintenance bay where the airflow is not strong and directional. This also enhances the velocity contours around the PAPR, enabling the visualizations of streamlines of particle motion around the PAPR.

Table 5. Simulation procedure

Time (s)	Activity
1–15	Let air velocity stabilize
15–20	Inject particles at the five probe points
20–60	Let the PAPR capture the particles

It is important to note that the time steps were changed for all sets of transient-state simulations with varying inlet airflow speeds to ensure that the average Courant-Freidrichs-Lewy condition was met. We chose the time-step sizes accurately to keep the average Courant number under 1.00; this is shown in Table 6 and Figure 4.

Table 6. Courant number for all simulation cases

Inlet Velocity (m/s)	Time-Step (s)	Total time steps	CFL number
1.0	0.008	2,500	1.0000
1.5	0.005	4,000	0.9375
2.0	0.004	5,000	1.0000
2.5	0.003	6,667	0.9375
3.0	0.002	10,000	0.7500
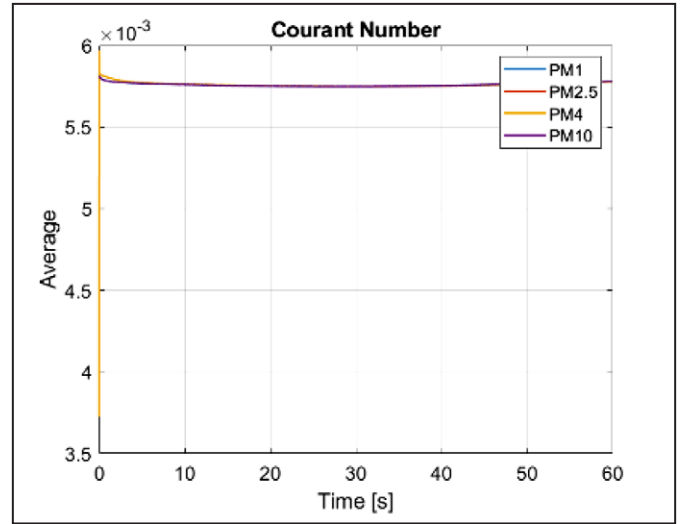
Figure 4. Courant number

We monitored the values of normalized wall distance (y+) throughout the simulations, which enabled us to determine the flow field resolution near the impermeable surfaces. Very low y+ values (Figure 5) show that the flow was resolved well.

RESULTS FROM THE CFD MODELS

We present the results from steady and transient-state simulations in the following sections.

STEADY-STATE SIMULATIONS

The residuals attained low values at the end of 500 iterations during the simulations. The simulations did not show any signs of divergence. We observed random fluctuations
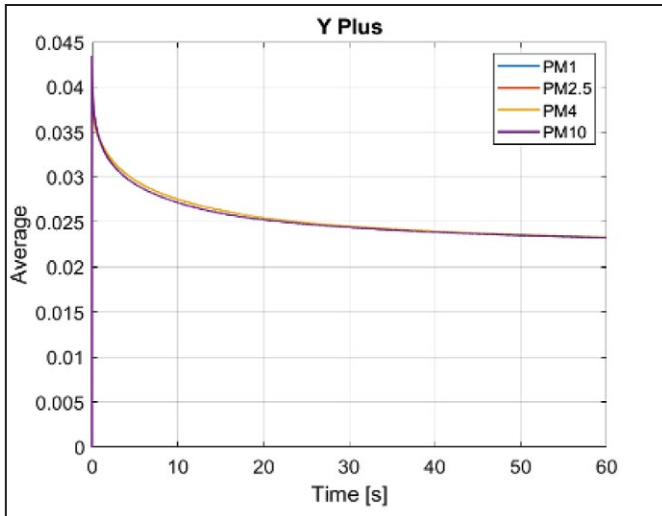
Figure 5. Normalized wall distance

in airflow contours near the PAPR inlet, which is most likely due to the steep gradients in the flow field near the PAPR. Using results from the simulations, we plotted the contours of velocity magnitude to identify the areas where particles might concentrate around the miner's head. Results are shown in Figures 6–8. The area at the back of the head shows a low-velocity profile in every case. Therefore, this region is expected to trap particles locally that will be captured by the PAPR. The effectiveness of the PAPR becomes progressively weaker as the ambient airflow speed is increased.

TRANSIENT-STATE SIMULATIONS

For the transient-state simulations, the inlet velocity was lowered to 0.01 m/s, and an outlet airflow of 170 L/min was added to the back of the head to capture the particles. This airflow is representative of the flow through a typical Versaflow PAPR. Particles were injected at the five probe points at a rate of 0.0013 kg/s. This corresponds to a concentration of 4.08 mg/m^3 in our domain, which is the continuous miner operator's exposure as obtained from the literature [16]. Many graphs were plotted for each particle size. First, the velocities at the probe points were used to monitor the state of the flow. Figure 9 shows one such graph where airflow velocity is plotted at those probe points for PM10. Similar graphs were plotted for other particle sizes. The velocity magnitude remained the same for all particle sizes. This indicates that the airflow momentum dominates the particulate transportation despite a bi-directional coupling.

Finally, the mass flows were plotted to understand the behavior of the particles under these specific conditions.
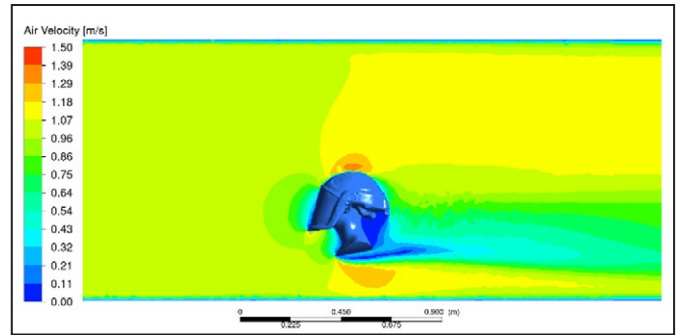

Figure 6. Contours of velocity magnitude on a plane through the PAPR for an inlet velocity of 1.0 m/s
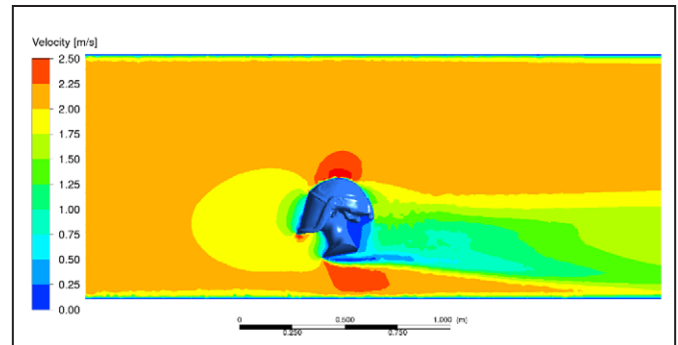

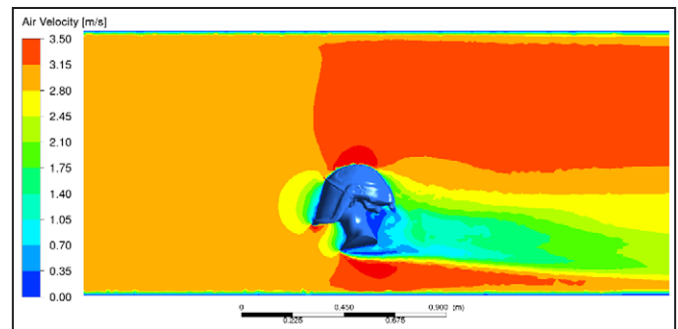**Figure 7. Contours of velocity magnitude for an inlet velocity of 2.0 m/s**

Figure 8. Contours of velocity magnitude for an inlet velocity of 3.0 m/s

Figure 10–13 represent the mass flow rates of injected particles and the escaped particles through the control surface at the back of the PAPR. As particles were injected at specific points around the PAPR, it was expected that the escaped particles graph would show different waves of particles escaping the domain, meaning that the particles were being carried by the airflow from the different injection points. Integrating the graph, it is possible to obtain the mass balance after the first minute of operation. This is shown in Table 7.
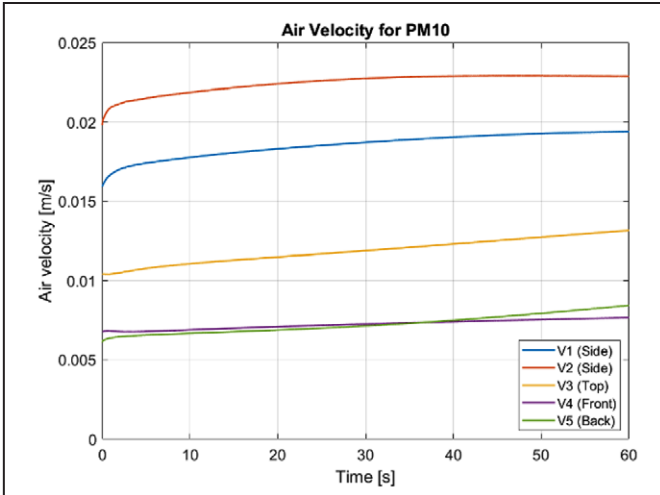
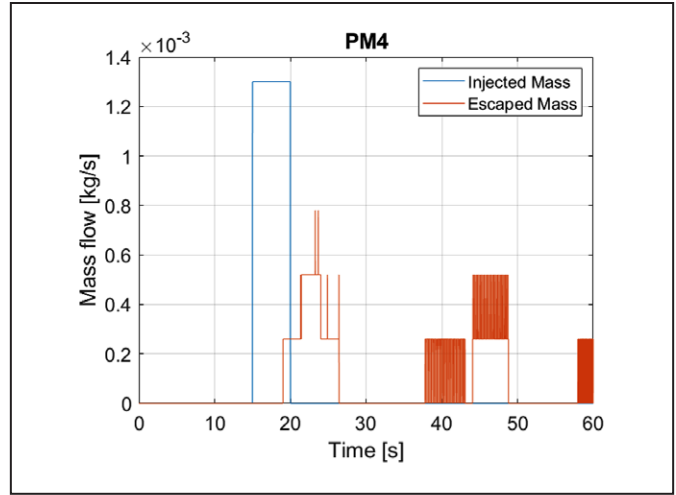**Figure 9. Air velocity magnitude at the five probe points**

Figure 12. Plot of injected and escaped mass of PM4 particulates from the flow domain
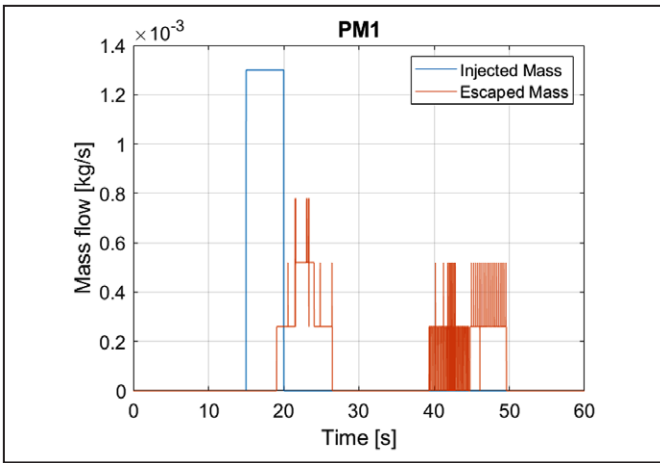

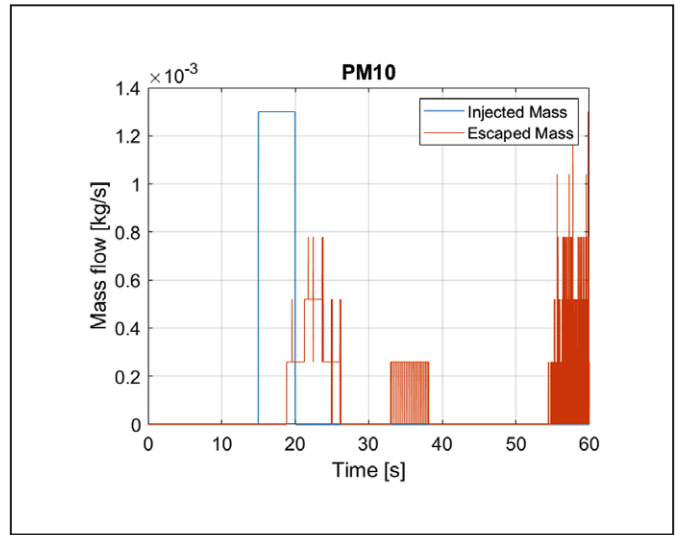**Figure 10. Plot of injected and escaped mass of PM1 particulates from the flow domain**

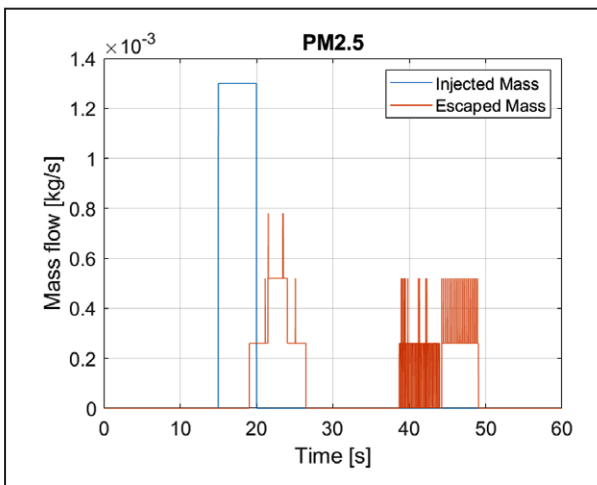**Figure 13. Plot of injected and escaped mass of PM10 particulates from the flow domain**

Table 7. Injected and captured mass through the PAPR

Particle Size	Injected Mass (kg)	Captured Mass (kg)	Capture Efficacy (%)
PM1	0.0065	0.0052	80.00
PM2.5	0.0065	0.0052	80.00
PM4	**0.0065**	**0.0057**	**87.69**
PM10	**0.0065**	**0.0050**	**76.29**

CONCLUSIONS AND FUTURE WORK

PAPRs are a class of PPEs that were shown to have high protection factors in preventing the exposure of medical personnel during the COVID-19 pandemic. It uses a HEPA filter to capture aerosols that could be respirable.

Figure 11. Plot of injected and escaped mass of PM2.5 particulates from the flow domain

We propose a widespread application of these respirators in the mining industry where miners have been conclusively shown to have suffered from several forms of pneumoconiosis.

As the first step to establishing their efficacy in an underground mine environment, we developed CFD simulations to demonstrate the flow field around a miner who has donned a PAPR. A LiDAR scan was used to develop the complicated geometry of the miner with a PAPR. The LiDAR scan eliminated the need to approximate any geometrical features. Through these numerical simulations, we established the procedure to replicate different operating conditions for a PAPR in a confined volume. Steady-state simulations enabled us to visualize the airflow patterns around the PAPR and regions of recirculation, and transient-state models enabled us to determine different parameters such as particulate positions and airflow velocity. We showed that under low directional airflow in a confined space, the PAPR can generate adequate airflow to capture particulates. However, the models also demonstrate visually that airflow through the PAPR is not strong enough to attract respirable particulates toward itself to capture them on an active mining face as it is restricted by human breathing and motor power.

This was the first approach that was taken to the modeling of PAPRs in underground mining tunnels. The simulations show the ability of the CFD models to accurately predict conditions and help researchers understand the conditions under which a PAPR's use will be most efficient. Future work includes the validation of results and running longer simulations to predict the absolute amount of particles captured by the PAPR during its 8-hour battery life. While running steady-state and transient cases, many of the impacts of the airflow were understood. The position of the inlet and outlets will be improved for the next steps. Some adjustments will be made to the geometry to achieve even more realistic conditions, and the flow parameters will also be adjusted to replicate the conditions of a mine.

ACKNOWLEDGMENTS

REFERENCES

[1] Y. Shekarian, E. Rahimi, M. Rezaee, W.C. Su, and P. Roghanchi, "Respirable coal mine dust: a review of respiratory deposition, regulations, and characterization," Minerals, vol. 11, p. 696, 2021.

[2] J. Colinet, C. N. Halldin, and J. Schall, Best practices for dust control in coal mining, 2021.

[3] A. R. Kumar and S. Schafrik, "Multiphase CFD modeling and laboratory testing of a Vortecone for mining and industrial dust scrubbing applications," Process Safety and Environmental Protection, vol. 144, pp. 330–336, 2020.

[4] A. R. Kumar, N. Gupta, and S. Schafrik, "CFD modeling and laboratory studies of dust cleaning efficacy of an efficient four-stage non-clogging impingement filter for flooded-bed dust scrubbers," International Journal of Coal Science & Technology, vol. 9, no. 1, p. 16, 2022.

[5] NIOSH, "Niosh-approved p100 particulate filtering facepiece respirators," 11 2024. [Online]. Available: https://www.cdc.gov/niosh/npptl/topics/ respirators/ disp part/p100list1.html.

[6] M. D. of Health, "Powered air purifying respirator (PAPR)," 2022.

[7] V. Roberts, "To PAPR or not to PAPR?" Canadian Journal of Respiratory Therapy: CJRT= Revue canadienne de la therapie respiratoire: RCTR, vol. 50, p. 87, 2014.

[8] J. Schumacher, S. A. Gray, L. Weidelt, A. Brinker, K. Prior, and W. M. Stratling, "Comparison of powered and conventional air-purifying respirators during simulated resuscitation of casualties contaminated with hazardous substances," Emergency medicine journal, vol. 26, pp. 501–505, 2009.

[9] N. J. Bollinger, "NIOSH respirator selection logic," 2004.

[10] S. S. Xu, Z. Lei, Z. Zhuang, and M. Bergman, "Computational fluid dynamics simulation of flow of exhaled particles from powered-air purifying respirators," in International Design Engineering Technical Conferences and Computers and Information in Engineering Conference, vol. 59179. American Society of Mechanical Engineers, 2019.

[11] M. Bergman, Z. Lei, S. Xu, K. Strickland, and Z. Zhuang, "Validation of computational fluid dynamics models for evaluating loose-fitting powered air-purifying respirators," in Proceedings of the 20th Congress of the International Ergonomics Association (IEA 2018) Volume II: Safety and Health, Slips, Trips and Falls 20. Springer, 2019, pp. 176–185.

[12] S. I. Cheberiachko, D. V. Slavinskyi, Y. I. Cheberiachko, and O. V. Deryugin, "Mathematical model of air flow movement in a motorized filter respirator," Natsional'nyi Hirnychyi Universytet. Naukovyi Visnyk, pp. 97–103, 2023.

[13] M. Cagna and M. Boehle, "Application of CFD methods for the simulation of the flow through a filter in dependency of the operating time," in Fluids Engineering Division Summer Meeting, vol. 36150, 2002, pp. 1013–1017.

[14] C. Yue, Q. Zhang, and Z. Zhai, "Numerical simulation of the filtration process in fibrous filters using CFD-DEM method," Journal of Aerosol Science, vol. 101, pp. 174–187, 2016.

[15] Özgün, "Ansys mesh metrics explained," 2023. [Online]. Available: https://www.mechead.com/mesh-quality-checking-ansys-workbench/.

[16] H. N. Doyle, "Dust concentration in the mines," Information Circular, no. 8458–8462, p. 27, 1970.